Appl Magn Reson (2017) 48:749–760
DOI 10.1007/s00723-017-0910-0

Applied
Magnetic Resonance

ORIGINAL PAPER

Compressed Sensing MRI Using Sparsity Averaging and FISTA

Jian-ping Huang[1] · Liang-kuan Zhu[1] · Li-hui Wang[2] · Wen-long Song[1]

Received: 24 March 2017 / Published online: 27 June 2017

Abstract Magnetic resonance imaging (MRI) is widely adopted for clinical diagnosis due to its non-invasively detection. However, acquisition of full k-space data limits its imaging speed. Compressed sensing (CS) provides a new technique to significantly reduce the measurements with high-quality MR image reconstruction. The sparsity of the MR images is one of the crucial bases of CS-MRI. In this paper, we present to use sparsity averaging prior for CS-MRI reconstruction in the basis of that MR images have average sparsity over multiple wavelet frames. The problem is solved using a Fast Iterative Shrinkage Thresholding Algorithm (FISTA), each iteration of which includes a shrinkage step. The performance of the proposed method is evaluated for several types of MR images. The experiment results illustrate that our approach exhibits a better performance than those methods that using redundant frame or a single orthonormal basis to promote sparsity.

1 Introduction

Magnetic resonance imaging (MRI) is widely adopted for the clinical diagnosis due to its non-invasively detection technique. However, the imaging speed of MRI is often limited. One of the most important influence factors is the amount of k-space data that need to be acquired. Therefore, accelerating the acquisition of MRI is still a great challenge for certain clinical applications. To address this issue, numerous research works have been reported, such as designing imaging sequences for fast acquisition and

✉ Jian-ping Huang
jianping829@gmail.com

[1] College of Mechanical and Electrical Engineering, Northeast Forestry University, Harbin 150040, Heilongjiang Province, China

[2] College of Computer Science and Technology, Guizhou University, Huaxi District, Guiyang 550025, China

maintaining reconstruction image quality with the acquisition data as few as possible [1–5]. Among them, parallel imaging (PI) emerged as the most widely used technique in clinical routine [5], including sensitivity encoding (SENSE) [2], simultaneous acquisition of spatial harmonics (SMASH) [6], generalized auto calibrating partially parallel acquisitions (GRAPPA) [7], and iterative self-consistent parallel imaging reconstruction (SPIRiT) [8]. However, the PI techniques are typically limited by Nyquist sampling rate and the achieved acceleration is limited to low factor values [9].

The compressed sensing (CS) [10, 11] is a new technique which has recently emerged as powerful approach for both acquiring data and reconstructing signals with high quality from highly under-sampled measurements (with respect to the traditional Shannon–Nyquist sampling theorem required). CS is a new promising method which is able to reconstruct high-quality MR images from highly under-sampled k-space data, called the CS-MRI, which assumes that MR images can be represented sparsely in image or transform domain. Consequently, CS-MRI allows to reconstructing the images from much less measurements compared with the conventional methods, and to reducing MRI scanning time efficiently without degrading image quality [9, 12, 13]. The first work of CS-MRI was proposed in [12], which employed two commonly sparsifying transforms as sparsity constraint, namely total variation (TV) and discrete wavelet transform (DWT). According to structured sparsity theory, the wavelet tree structure has been proposed in [14] for CS-MRI, which can be further improved the reconstruction MR image quality than standard wavelet sparsity prior. However, MR images usually have more sparse representation in a redundant dictionary, such as redundant wavelet transform [15], contourlet [16], framelets [17], and shearlet [18]. Instead of predefined transforms, much ongoing work for CS-MR image reconstruction is based on data-adaptive sparsifying transform, such as singular value decomposition (SVD) [19], dictionary learning [20–23], and patch-based adaptive kernel methods [24, 25].

In this study, we present to use sparsity averaging prior for CS-MRI in the basis of that MR images have average sparsity over multiple wavelet frames. The problem is solved using a fast iterative shrinkage thresholding algorithm (FISTA), each iteration of which includes a shrinkage step. The performance of the proposed approach was evaluated for several types of MR images. The experiment results illustrate that our method exhibits better performance than those methods that using redundant frame or a single orthonormal basis to promote sparsity.

2 Methodology

2.1 CS-MRI

Compressed sensing (CS) [10, 11] methods are able to reconstruct MR images with high quality from much fewer k-space data, consequently, which make it possible to reduce MRI acquisition time efficiently [13]. Given an observation vector y in k-space domain and the sensing matrix Φ, the purpose of CS-MRI is to reconstruct the MR image x with $y = \Phi x$ by solving an optimization problem as follows:

$$\min_{x \in \mathbb{R}^n} \|x\|_0 \quad s.t. \;\; y = \Phi x. \tag{1}$$

However, the problem in Eq. (1) involves the l_0 norm which requires combinatorial optimization. Fortunately, if the potential image x is sufficiently sparse in some domain [11], it is possible to replace the l_0 norm by the l_1 norm (represents the sum of absolute values of each element in a vector) in Eq. (1) without degrading reconstruction image quality. Then, the minimization problem Eq. (1) is reformulated as:

$$\min_{x\in\mathbb{R}^n}\|x\|_1 \quad s.t. \;\; y=\Phi x. \tag{2}$$

2.2 The Proposed Method

The sparsity of the MR images is one of the crucial bases for CS-MRI. In this study, we propose to use the sparsity averaging prior [26] for CS-MRI reconstruction based on the fact that MR images have average sparsity over multiple wavelet frames. Then, the CS-MR image reconstruction problem can be written as:

$$\widetilde{x}=\arg\min_{x}\|y-\Phi x\|_2+\lambda\left\|W\Psi^{\dagger}x\right\|_1 \tag{3}$$

where Φ is a partial Fourier transform expressed by $F_u = P\cdot F$, and F represents Fourier transform, P is common under-sampling pattern (mask); $W\in\mathbb{C}^{D\times D}$ is a positive diagonal weighting matrix; $\Psi=\frac{1}{\sqrt{q}}\left[\Psi_1,\Psi_2,\ldots,\Psi_q,\right]\in\mathbb{C}^{N\times D}$, $N<D$ is a dictionary which is composed of frame concatenation Ψ_i with $1\le i\le q$.

Let $f(x)=\frac{1}{2}\|y-Ax\|_2^2$, which is a convex and smooth function with Lipschitz L_{f}, and $g(x)=\lambda\|W\Psi^{\dagger}x\|_1$, which is convex but non-smooth function. Then, Eq. (3) can be solved by the FISTA [27]. The pseudocode of the presented method is indicated in Algorithm FSACSMRI, where $\nabla f\left(r^k\right)=\Phi^T(y-\Phi x)$ with Φ^T denotes the inverse partial Fourier transform; the proximal map is defined for any scaler $\rho>0$:

$$prox_{\rho}(f)(x)=\arg\min_{u}\left\{f(v)+\frac{1}{2\rho}\|v-x\|_2^2\right\}. \tag{4}$$

Algorithm FSACSMRI

INPUT: $\rho=1/L_f,\lambda,t^1=1,x^0=r^1$

FOR k = 1 **TO** K **DO**

$$x_g=r^k-\rho\nabla f\left(r^k\right);$$

$$x^k=prox_{\rho}\left(2\lambda\left\|W\Psi^{\dagger}x\right\|\right)\left(x_g\right);$$

$$x^k=\mathrm{project}\left(x^k,[l,u]\right);$$

$$t^{k+1}=\frac{1+\sqrt{1+4\left(t^k\right)^2}}{2};$$

$$r^{k+1}=x^k+\frac{t^k-1}{t^{k+1}}\left(x^k-x^{k-1}\right);$$

END

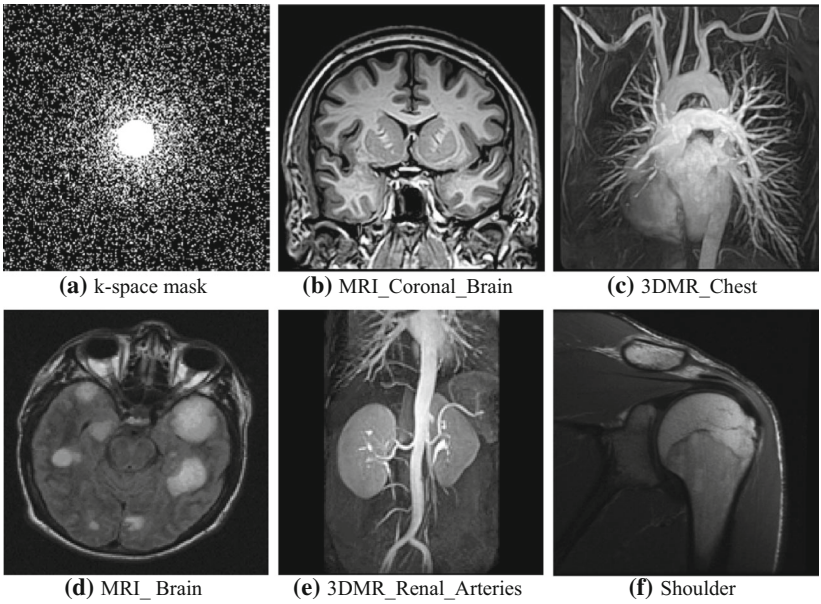

Fig. 1 Under-sampling mask and test images

3 Results and Discussion

3.1 Materials

To compare with the conventionally used sparsifying transforms in the CS-MRI, two-dimensional (2D) MR images with dimension of 256 $\times$ 256 are used in present work (these images can be download from Ref. [28]), as illustrated in Fig. 1. Figure 1a indicates the k-space under-sampling mask with a under-sampled ratio of 20% using the variable density sampling pattern [12]. Figure 1b–f illustrates the original MR images which are acquired with full k-space data and considered as the ground truth for comparing the proposed method with other approaches. In the experiments, we use Daubechies wavelets with four decomposition levels for sparsifying image. All codes of the other methods are downloaded from the authors' websites for fair comparisons. The observation noise standard deviation ε is set to 0.01 and the regularization parameter $\lambda = 0.035$.

For evaluating the performance of the method presented in this work, we compare it with several CS-MRI reconstruction approaches, including the SparseMRI [12], Contourlet [16], FCSA [28], and WaTMRI [29]. The indices including mean structural similarity (MSSIM) and peak-signal-to-noise ratio

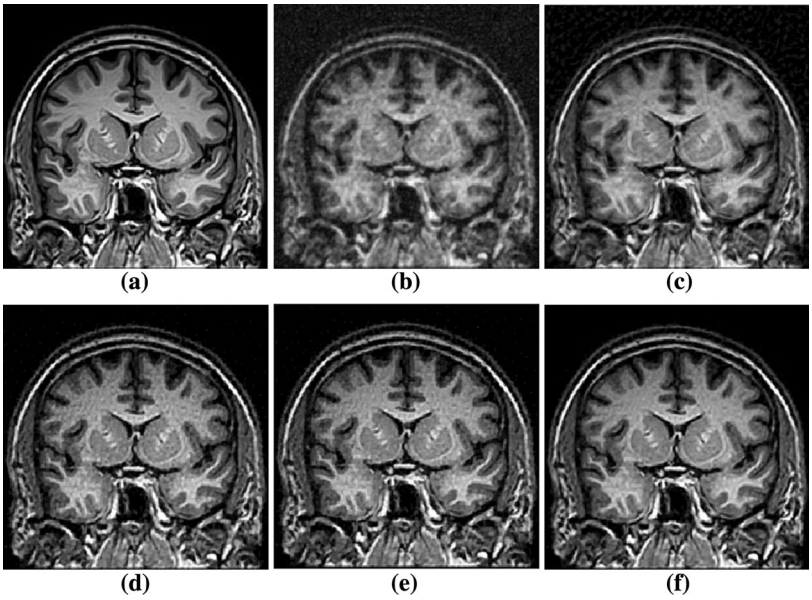

Fig. 2 Reconstructed MR images using different methods with 20% sampling. **a** Original MR images of MRI coronal brain; images reconstructed by **b** SparseMRI [12]; **c** Contourlet [16]; **d** FCSA [28]; **e** WaTMRI [29]; **f** FSACSMRI (proposed)

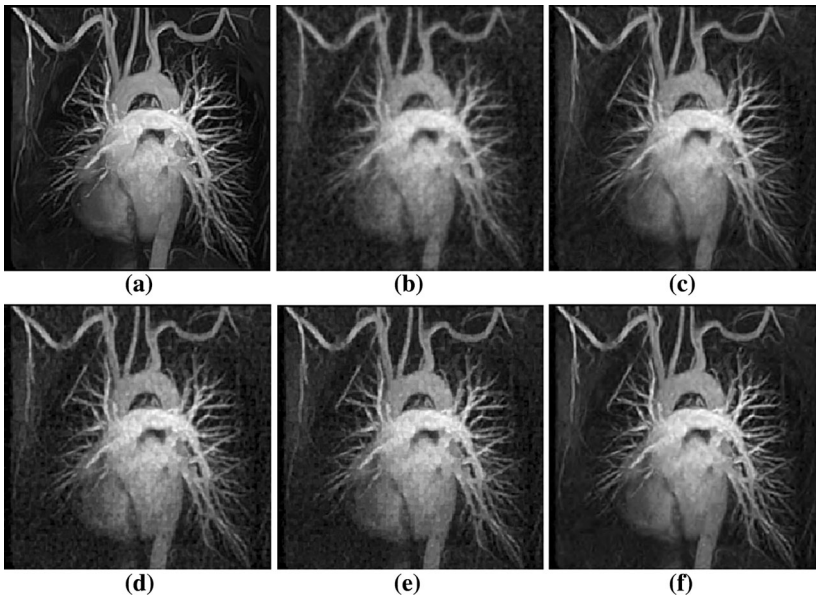

Fig. 3 Reconstructed MR images using different methods with 20% sampling. **a** Original MR images of 3DMR Chest; images reconstructed by **b** SparseMRI [12]; **c** Contourlet [16]; **d** FCSA [28]; **e** WaTMRI [29]; **f** FSACSMRI (proposed)

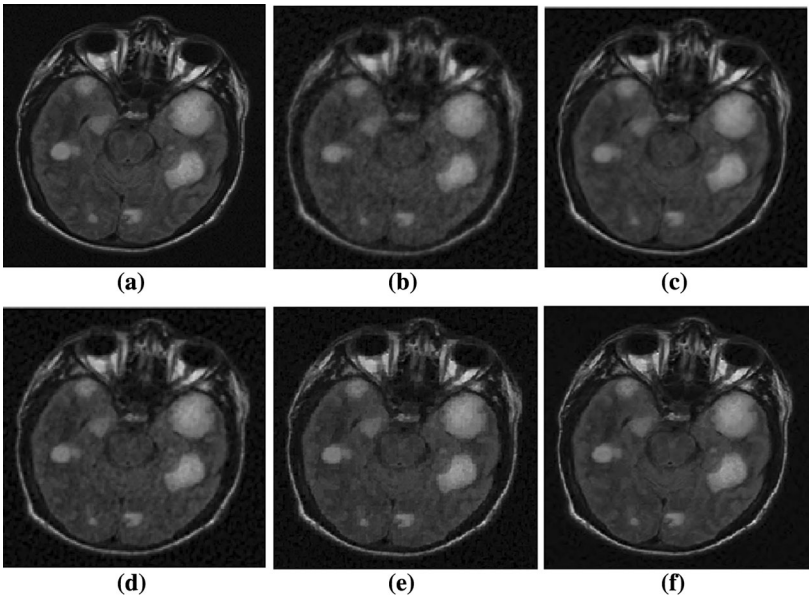

Fig. 4 Reconstructed MR images using different methods with 20% sampling. **a** Original MR images of MRI Brain; images reconstructed by **b** SparseMRI [12]; **c** Contourlet [16]; **d** FCSA [28]; **e** WaTMRI [29]; **f** FSACSMRI (proposed)

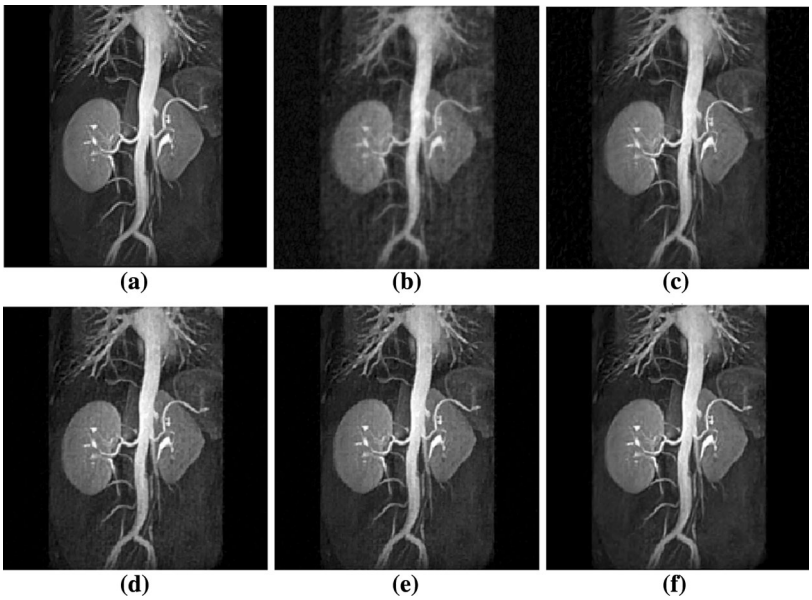

Fig. 5 Reconstructed MR images using different methods with 20% sampling. **a** Original MR images of 3DMR Renal Arteries; images reconstructed by **b** SparseMRI [12]; **c** Contourlet [16]; **d** FCSA [28]; **e** WaTMRI [29]; **f** FSACSMRI (proposed)

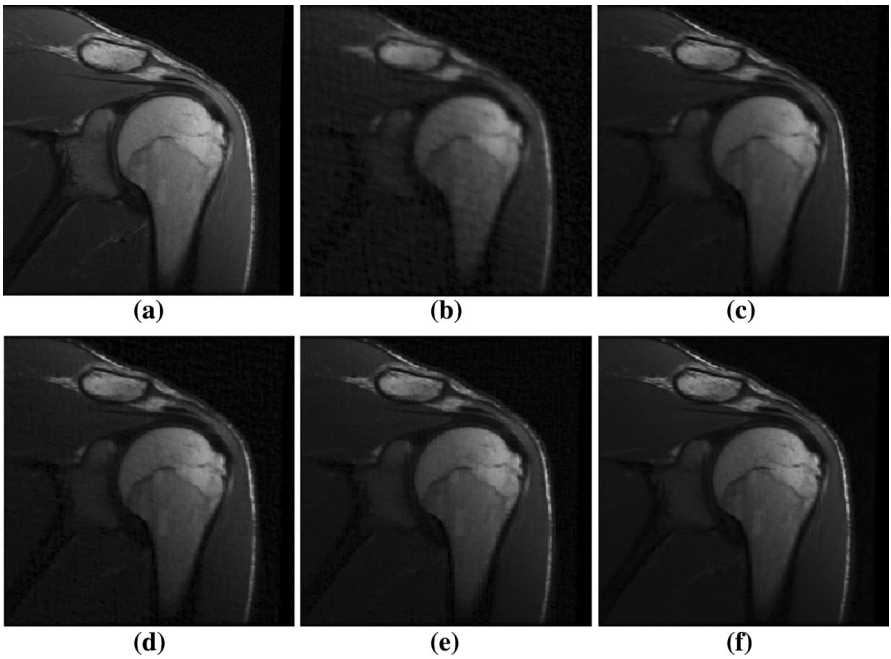

Fig. 6 Reconstructed MR images using different methods with 20% sampling. **a** Original MR images of shoulder; images reconstructed by **b** SparseMRI [12]; **c** Contourlet [16]; **d** FCSA [28]; **e** WaTMRI [29]; **f** FSACSMRI (proposed)

(PSNR) [30] are also derived for comparing these methods quantitatively. The PSNR is defined as:

$$\mathrm{PSNR} = 20\log_{10}\left(\frac{MAX_x}{\sqrt{MSE}}\right) \tag{5}$$

where $\mathrm{MSE} = \frac{1}{M\times N}\sum_{i=1}^{M}\sum_{j=1}^{N}\left[x_{ref}(i,j) - x_{rec}(i,j)\right]^2$; MAX_x is the maximum possible pixel value of the image, which is set to be 1 or 255.

The SSIM is formulated as [30]:

$$\mathrm{SSIM}(x,y) = \frac{\left(2\mu_x\mu_y + C_1\right)\left(2\sigma_{xy} + C_2\right)}{\left(\mu_x^2 + \mu_y^2 + C_1\right)\left(\sigma_x^2 + \sigma_y^2 + C_2\right)} \tag{6}$$

where the parameters C_1 and C_2 are constants that avoid instability when the local means μ_x and μ_y, and local standard deviations σ_x and σ_y are close to zero. The mean SSIM (MSSIM) is a single value that represents an overall quality measure of the entire image. The MSSIM values exhibit much better consistency with qualitative visual appearance [30].

Table 1 PSNR of reconstruction using different methods with 20% sampling

Image	SparseMRI	Contourlet	FCSA	WaTMRI	Proposed
Coronal brain	20.70	23.77	27.34	27.41	29.48
3DMR chest	25.26	28.30	27.82	28.56	31.37
MRI brain	28.83	32.73	32.03	33.07	37.08
3DMR renal arteries	26.63	30.93	33.42	34.26	37.28
Shoulder	32.89	39.20	38.66	39.84	45.79

Table 2 MSSIM of reconstruction using different methods with 20% sampling

Image	SparseMRI	Contourlet	FCSA	WaTMRI	Proposed
Coronal brain	0.55	0.69	0.88	0.88	0.92
3DMR chest	0.68	0.78	0.75	0.78	0.87
MRI brain	0.78	0.86	0.83	0.87	0.94
3DMR renal arteries	0.54	0.76	0.90	0.92	0.95
Shoulder	0.86	0.95	0.94	0.95	0.98

3.2 Visual comparisons

Figures 2, 3, 4, 5, 6 give the visual comparisons of the several types of MR images reconstructed from different methods. The under-sampled ratio is about 20%. From such figures, we observe that the image reconstructed with the method proposed in this work has sharp contours and edges and gives fine image details.

To provide more intuitive result, the PSNR and MSSIM indices for MR images reconstructed from 20% k-space data with different methods are compared quantitatively, as shown in Tables 1 and 2, respectively. It indicates that our method has the highest PSNRs and the greatest MSSIMs.

Figures 7, 8 give the curve of PSNR and MSSIM versus different under-sampled ratio (10–50% or 0.10–0.50) for the MR images reconstructed with different methods. It can be seen that the FCSA and WaTMRI have a similar performance for the Coronal Brain MR image, and our method has always a better performance than SparseMRI, Contourlet, FCSA, and WaTMRI in terms of PSNR and MSSIM for different MR images.

Figure 9 gives the comparison reconstruction time between the proposed method and the other methods with different under-sampled ratio and different images. From the figures, it can be clearly observed that the FCSA and WaTMRI methods are the fastest among the five methods, and the proposed method takes the longer reconstruction time. On the other hand, the computation time of the methods has no obvious change for different images and different under-sampled ratio.

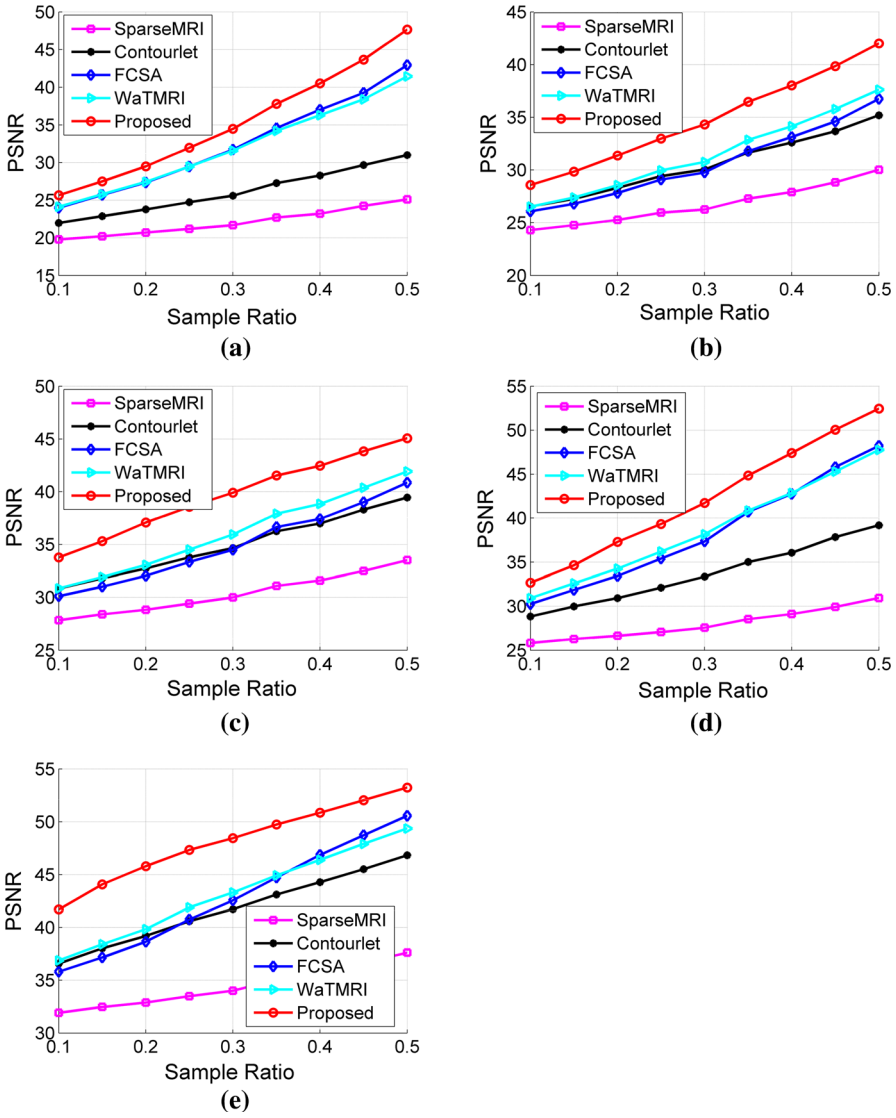

Fig. 7 Performance comparisons (PSNR vs. different sampling rates) for different MR images reconstructed with different methods: **a** coronal brain image; **b** 3DMR chest image; **c** MRI brain; **d** 3DMR renal arteries; **e** shoulder

4 Conclusions

In this study, we introduced an approach for CS-MR image reconstruction by employing sparsity averaging constraint as powerful prior, which promotes average signal sparsity over multiple wavelet basis. The experiment results illustrate that our

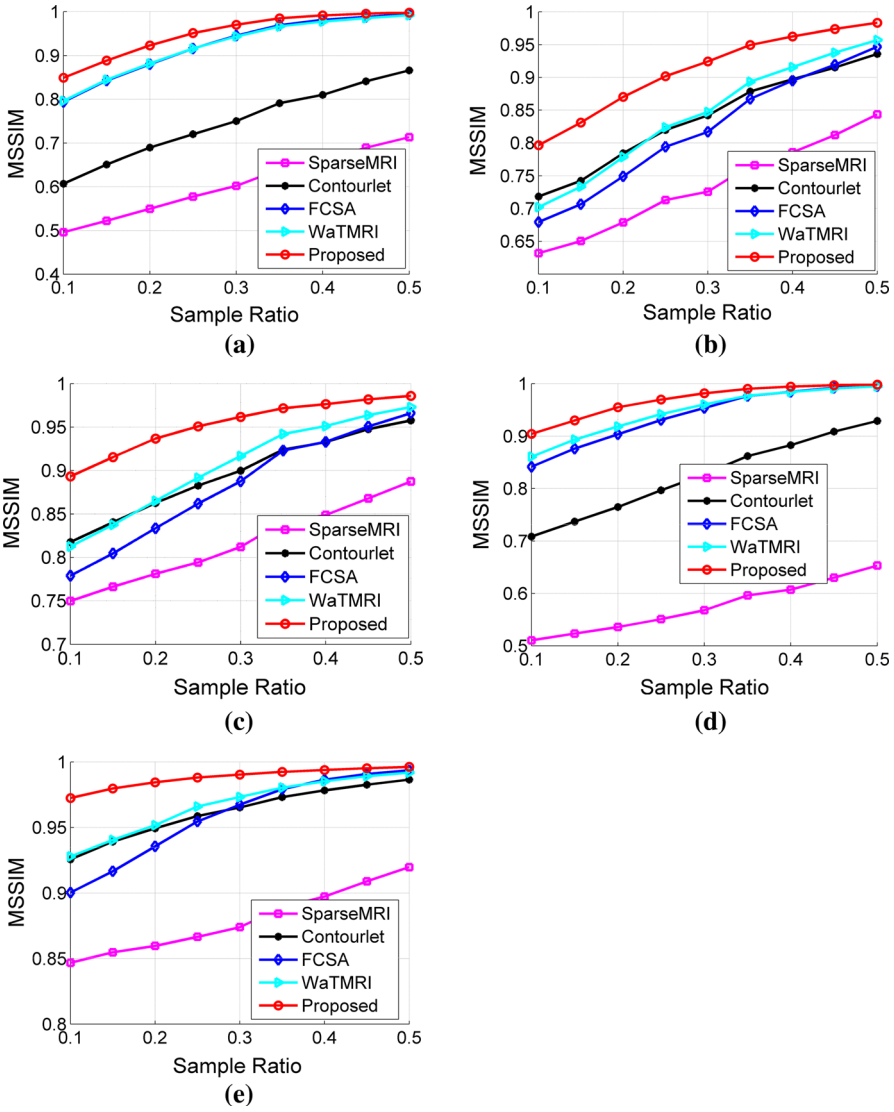

Fig. 8 Performance comparisons (MSSIM vs. different sampling rates) for different MR images reconstructed with different methods: **a** Coronal brain image; **b** 3DMR chest image; **c** MRI brain; **d** 3DMR renal arteries; **e** shoulder

approach exhibits a better reconstruction performance compared to state-of-the-art CS-MRI reconstruction methods. In addition, the image quality reconstructed with our method is not sensitive to the under-sampling rates for different types of MR images, which illustrates the robustness of such approach.

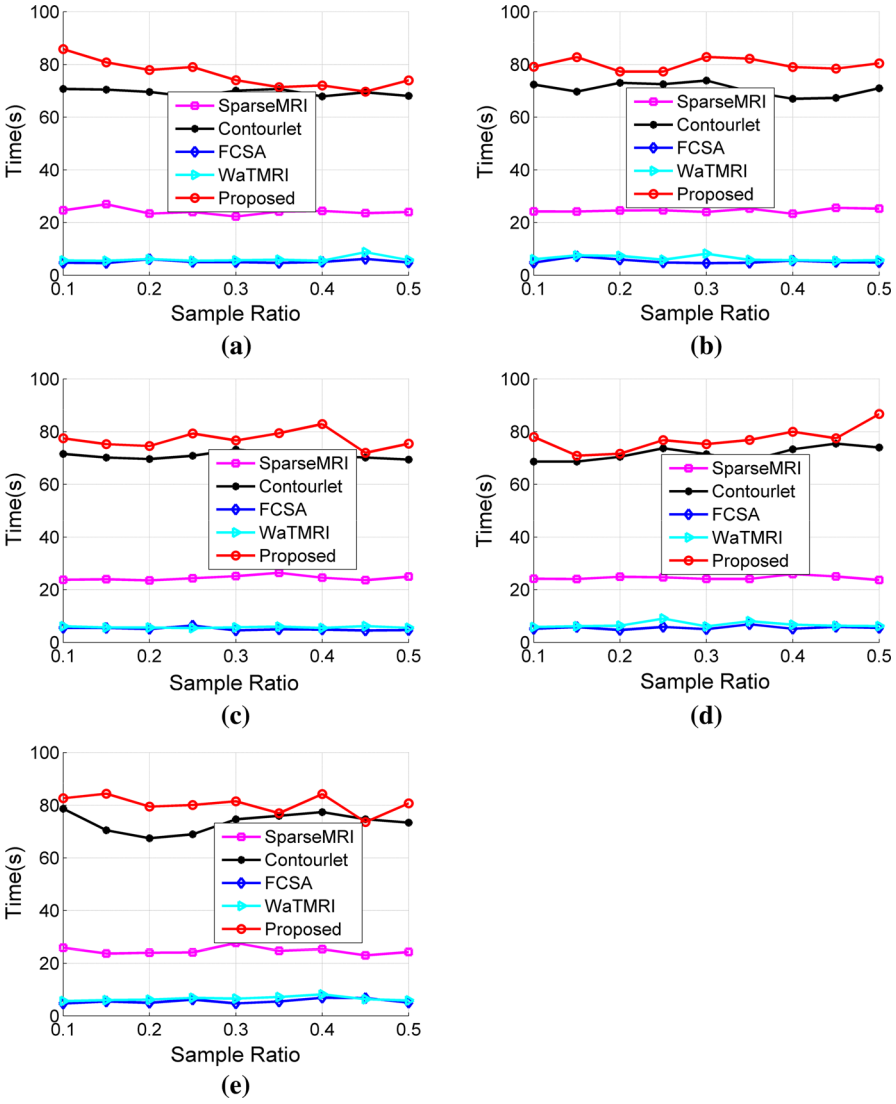

Fig. 9 Performance comparisons [times (unit second) vs. different sampling rates] for different MR images reconstructed with different methods: **a** coronal brain image; **b** 3DMR chest image; **c** MRI brain; **d** 3DMR renal arteries; **e** shoulder

Acknowledgements This study was supported by the Fundamental Research Funds for the Central Universities, China (No. 41112414), and the National Natural Science Foundation of China (Nos. 31470714, 31370710, 61661010).

References

1. G. McGibney, M.R. Smith, S.T. Nichols, A. Crawley, Magn. Reson. Med. **30**(1), 51–59 (1993)

2. K.P. Pruessmann, M. Weiger, M.B. Scheidegger, P. Boesiger, Magn. Reson. Med. **42**(5), 952–962 (1999)
3. J. Tsao, S. Kozerke, J. Magn. Reson. Imaging **36**(3), 543–560 (2012)
4. J. Luo, Y. Zhu, W. Li, P. Croisille, I.E. Magnin, J. Magn. Reson. Imaging **35**(5), 1196–1206 (2012)
5. D.J. Larkman, R.G. Nunes, Phys. Med. Biol. **52**(7), R15–R55 (2007)
6. D.K. Sodickson, W.J. Manning, Magn. Reson. Med. **38**(4), 591–603 (1997)
7. M.A. Griswold, P.M. Jakob, R.M. Heidemann, M. Nittka, V. Jellus, J.M. Wang, B. Kiefer, A. Haase, Magn. Reson. Med. **47**(6), 1202–1210 (2002)
8. M. Lustig, J.M. Pauly, Magn. Reson. Med. **64**(2), 457–471 (2010)
9. K.G. Hollingsworth, Phys. Med. Biol. **60**(21), R297 (2015)
10. E.J. Candes, J. Romberg, T. Tao, IEEE Trans. Inf. Theory **52**(2), 489–509 (2006)
11. D.L. Donoho, IEEE Trans. Inf. Theory **52**(4), 1289–1306 (2006)
12. M. Lustig, D. Donoho, J.M. Pauly, Magn. Reson. Med. **58**(6), 1182–1195 (2007)
13. M. Lustig, D.L. Donoho, J.M. Santos, J.M. Pauly, IEEE Signal Process. Mag. **25**(2), 72–82 (2008)
14. C. Chen, J. Huang, Med. Image Anal. **18**(6), 834–842 (2014)
15. Z. Lai, X. Qu, Y. Liu, D. Guo, J. Ye, Z. Zhan, Z. Chen, Med. Image Anal. **27**, 93–104 (2016)
16. X. Qu, W. Zhang, D. Guo, C. Cai, S. Cai, Z. Chen, Inverse Prob. Sci. Eng. **18**(6), 737–758 (2010)
17. V.P. Gopi, P. Palanisamy, K.A. Wahid, P. Babyn, Int. J. Comput. Assist. Radiol. Surg. **9**(3), 459–472 (2014)
18. Q. Jing, G. Weihong, in *2013 IEEE 10th International Symposium on Biomedical Imaging: From Nano to Macro (ISBI 2013)*, pp. 306–309 (2013)
19. M. Hong, Y. Yu, H. Wang, F. Liu, S. Crozier, Phys. Med. Biol. **56**(19), 6311–6325 (2011)
20. S. Ravishankar, Y. Bresler, IEEE Trans. Med. Imaging **30**(5), 1028–1041 (2011)
21. Y. Chen, X. Ye, F. Huang, Inverse Prob. Imaging **4**(2), 223–240 (2010)
22. M. Doneva, P. Boernert, H. Eggers, C. Stehning, J. Senegas, A. Mertins, Magn. Reson. Med. **64**(4), 1114–1120 (2010)
23. J. Huang, L. Guo, Q. Feng, W. Chen, Y. Feng, Phys. Med. Biol. **60**(14), 5359–5380 (2015)
24. J.F.M. Schmidt, C. Santelli, S. Kozerke, PLoS One **11**(4), e0153736 (2016)
25. J. Zhang, D. Zhao, W. Gao, IEEE Trans. Image Process. **23**(8), 3336–3351 (2014)
26. R.E. Carrillo, J.D. McEwen, Y. Wiaux, Mon. Not. R. Astron. Soc. **426**(2), 1223–1234 (2012)
27. A. Beck, M. Teboulle, SIAM J. Imaging Sci. **2**(1), 183–202 (2009)
28. J. Huang, S. Zhang, D. Metaxas, Med. Image Anal. **15**(5), 670–679 (2011)
29. C. Chen, J. Huang, in *Advances in neural information processing systems*, vol. 25, pp. 1124–1132 (2012)
30. Z. Wang, A.C. Bovik, H.R. Sheikh, E.P. Simoncelli, IEEE Trans. Image Process. **13**(4), 600–612 (2004)